Thermal lensing, heat loading and power scaling of mid-infrared Er:CaF 2 lasers

Liza Basyrova, Pavel Loiko, Jean-Louis Doualan, Abdelmjid Benayad, Alain Braud, Bruno Viana, Patrice Camy

Research Article Vol. 30, No. 5 / 28 Feb 2022 / Optics Express 8092
Optics EXPRESS

Thermal lensing, heat loading and power scaling of mid-infrared Er:CaF_2 lasers

LIZA BASYROVA,[1] PAVEL LOIKO,[1] JEAN-LOUIS DOUALAN,[1] ABDELMJID BENAYAD,[1] ALAIN BRAUD,[1] BRUNO VIANA,[2] AND PATRICE CAMY[1,*]

[1] *Centre de Recherche sur les Ions, les Matériaux et la Photonique (CIMAP), UMR 6252 CEA-CNRS-ENSICAEN, Université de Caen Normandie, 6 Boulevard Maréchal Juin, 14050 Caen Cedex 4, France*
[2] *Chimie ParisTech, PSL University, CNRS, Institut de Recherche de Chimie Paris, 11 rue Pierre et Marie Curie, 75005 Paris, France*
[*] *patrice.camy@ensicaen.fr*

Abstract: Mid-infrared Er:CaF_2 laser operating on the $^4I_{11/2} \rightarrow {}^4I_{13/2}$ transition is developed. Its power scaling capabilities and thermo-optics (fractional heat loading and thermal lensing) are compared under pumping into the $^4I_{11/2}$ and $^4I_{9/2}$ states. Using a 4.5 at.% Er:CaF_2 crystal, a record-high continuous-wave output power of 0.83 W is achieved at 2800 nm with a slope efficiency of 31.6% and a laser threshold of 24 mW and the fractional heat loading is measured under lasing and non-lasing conditions, yielding the values of 52.0% and 71.7%, respectively (for pumping at 967.6 nm, into the $^4I_{11/2}$ state). The thermal lens in Er:CaF_2 is negative (divergent) owing to the negative thermo-optic coefficient and large and negative contribution of the photo-elastic effect. The sensitivity factors of the thermal lens are $M_r = -4.84$ and $M_\theta = -5.15$ [m^{-1}/(kW/cm^2)] and the astigmatism degree is as low as 6%. When pumping into the higher lying $^4I_{9/2}$ manifold, the thermal lens is enhanced owing to the additional heat generation from the multiphonon non-radiative path from this state, and the laser slope efficiency is deteriorated.

1. Introduction

Lasers emitting at the wavelengths of 2.7 - 3 μm falling into the mid-infrared spectral range are of practical importance for medicine. Such radiation is strongly absorbed by high moisture content materials such as biological tissues resulting in a small penetration depth and surgical precision of incisions. Lasers emitting at these wavelengths have been thus applied in "minimally invasive" dentistry [1], dermatology [2] and urology [3]. The 2.7 - 3 μm spectral range could be addressed by several rare-earth ions, such as Er^{3+}, Ho^{3+} and Dy^{3+}. Among them, the former ion could be easily pumped at ~0.96 μm, e.g., by commercial InGaAs diode lasers.

The mid-infrared emission of Erbium (Er^{3+}) around 2.8 μm originates from the $^4I_{11/2} \rightarrow {}^4I_{13/2}$ transition [4,5]. The latter has a self-terminating nature, i.e., the luminescence lifetime of the lower multiplet is longer than that of the upper one, making at a glance continuous-wave (CW) laser operation impossible. However, CW mid-infrared laser action from Er^{3+}-doped materials can be achieved using gain media ensuring a favorable ratio of upper state to lower state lifetimes, as well as efficient energy-transfer upconversion (ETU) process $^4I_{13/2} + {}^4I_{13/2} \rightarrow {}^4I_{15/2} + {}^4I_{9/2}$ depleting the lower laser level [6]. Longer lifetimes of the $^4I_{11/2}$ state are expected in low phonon energy materials which are less subject to multiphonon non-radiative (NR) relaxation. The condition of efficient ETU is typically reached by using high Er^{3+} doping levels (tens of at.% in crystals).

Among the host matrices for Er^{3+} doping, fluoride materials, such as glasses and single-crystals, appear attractive for mid-infrared lasers. CW lasing on the $^4I_{11/2} \rightarrow {}^4I_{13/2}$ transition has been demonstrated in Er:ZBLAN glasses [7,8] and Er:$LiYF_4$ [9], Er:BaY_2F_8 [10], Er:KY_3F_{10} [11],

#449129 https://doi.org/10.1364/OE.449129
Journal © 2022 Received 19 Nov 2021; revised 2 Jan 2022; accepted 13 Jan 2022; published 24 Feb 2022

Optics EXPRESS

Er:CaF_2 [12] and Er:SrF_2 [13] single-crystals. Wyss *et al.* reported on an Er:$LiYF_4$ laser operating at 2809 nm with a record-high slope efficiency of 50% well exceeding the Stokes limit and evidencing efficient ETU for optimized Er^{3+} doping [14]. Dergachev *et al.* reported on power scaling of a diode-pumped Er:$LiYF_4$ laser delivering up to 1.8 W at ~2810 nm at the expense of a lower slope efficiency of 13% [15]. Among the above-mentioned fluoride crystals, Er^{3+}-doped calcium fluoride (Er:CaF_2) attracts attention due to a unique combination of high thermal conductivity, broadband emission properties and efficient ETU even at low doping levels [12]. This crystal features a very strong clustering of rare-earth dopants (including Er^{3+} ions) already for >0.5 at.% doping leading to a significant inhomogeneous spectral broadening resulting in smooth and broad spectral bands (a glassy-like spectroscopic behavior) and efficient energy-transfer processes among the clustered dopants [16,17]. This makes Er:CaF_2 crystals very suitable for broadly tunable and ultrafast mid-infrared lasers (ensuring that the effect of the structured water vapor absorption in the air is eliminated, e.g., by gas purging).

Mid-infrared laser operation of Er:CaF_2 was studied previously, cf. Table 1 for a summary of the output characteristics [12,18–20,13,21]. In this table, the results are grouped according to the pump source (a Ti:Sapphire laser or a laser diode). Labbe *et al.* used a highly doped crystal (10.3 at.% Er:CaF_2) delivering 80 mW at 2800 nm with a slope efficiency of 30% under Ti:Sapphire laser pumping [12]. In [12], three pumping schemes for Er:CaF_2 lasers were proposed, namely pumping into the upper laser level $^4I_{11/2}$ (at ~0.97 μm), into the higher-lying multiplet $^4I_{9/2}$ (at ~0.80 μm) and into the terminal laser level $^4I_{13/2}$ (at ~1.54 μm), Fig. 1(a). Further power scaling was demonstrated by Ma *et al.* using a 4 at.% Er:CaF_2 crystal pumped by a laser diode and generating 304 mW however with a deteriorated slope efficiency of 17.2% and a much higher laser threshold of 335 mW mainly due to the poorer beam quality of the used pump source as compared to high-brightness laser pumping [19]. Much better laser performance was observed by Liu *et al.* using a compositionally "mixed" (solid-solution) crystal Er:(Ca,Sr)F_2: a diode-pumped laser generated 712 mW at 2732 nm with a high slope efficiency of 41.4% [22]. However, SrF_2-based crystals are out of the topic of the present work.

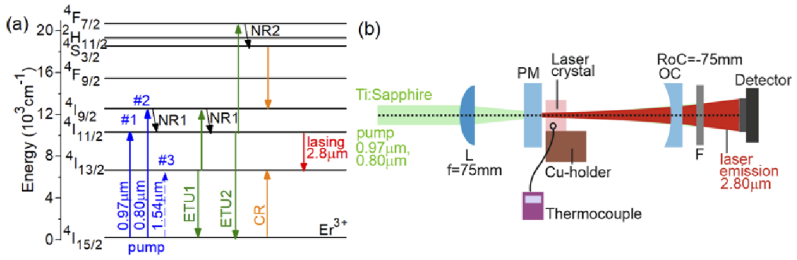

Fig. 1. (a) Energy-level scheme of Er^{3+} ions showing pump (*blue*) and laser (*red*) transitions, energy transfer upconversion (ETU, *green*), cross-relaxation (CR, *orange*) and non-radiative relaxation (NR, *black*) processes; (b) Scheme of the Er:CaF_2 laser: L, focusing lens, PM, pump mirror, OC, output coupler, F, long-pass filter.

Thermal lensing is an important effect for solid-state laser engineering as it affects the cavity stability and the mode-matching efficiency leading to deterioration of the laser performance. So far, thermo-optic effects have never been studied for mid-infrared Er:CaF_2 lasers. In this work, we aimed to study further power scaling capabilities and thermo-optics (including the astigmatic thermal lensing and the fractional heat loading) of ~2.8 μm Er:CaF_2 lasers for two commonly used pump schemes (pumping into the $^4I_{11/2}$ and $^4I_{9/2}$ Er^{3+} states), for the first time, to the best of our knowledge.

Optics EXPRESS

Table 1. Output Performance[a] of Mid-Infrared Er:CaF_2 Lasers Reported So Far

Pump	Er doping, at.%	Material	λ_P, nm	P_{out}, mW	λ_L, nm	η, %	P_{th}, mW	Ref.
LD	4.0	Crystal	974	282	2790	13.9	~240	[18]
	4.0	Crystal	972	304	-	17.2	335	[19]
	4.0	Crystal	974	295	2794	16.7	724	[20]
	5.0	Crystal	980[b]	~370	2747	5	~5000	[13]
	5.5	Ceramic	968	~4	2720	1.3	183	[21]
TS	10.3	Crystal	968	80	2800	30	**23**	[12]
	4.5	Crystal	967.6	**834**	2800	**31.6**	24	This work

[a]Pump: LD – laser diode, TS – Ti:sapphire laser, λ_P and λ_L – pump and laser wavelengths, respectively, P_{out} – output power, η – slope efficiency, P_{th} – laser threshold. [b]Transverse pumping.

2. Laser operation

2.1. Laser set-up

The Er:CaF_2 crystal was grown by the Bridgman technique. A mixture of high purity (4N) CaF_2 and ErF_3 powders was introduced in a graphite crucible. The growth chamber was sealed to a good vacuum ($<10^{-5}$ mbar) before introducing a mixture of Ar and CF_4 gases to avoid oxygen pollution. The furnace temperature was set to ~50 K above the melting point of CaF_2. After soaking, the charge was thoroughly melted, and the crystal growth was performed with a rate of 2–4 mm/h. After completing the growth, the crystal was slowly cooled down to room temperature within 48 hours. The actual Er^{3+} doping level in the crystal was determined by the inductively coupled plasma mass spectrometry (ICP-MS) method to be 4.5 at.% (ion density: $N_{Er} = 11.03\times10^{20}$ cm^{-3}). The crystal was oriented using a Laue diffractometer (ARL EQUINOX, Thermo Scientific). A rectangular laser element was cut along the [111] crystallographic direction having a thickness t of 7.0 mm. Both its input and output faces were polished to laser quality with a measured roughness in the nm-scale and left uncoated. This crystal cut was selected because of several reasons: (i) it is close to the crystal growth direction leading to better optical quality, (ii) it corresponds to lower depolarization losses and (iii) it provides lower thermal fracture probability.

The scheme of the laser set-up is shown in Fig. 1(b). The laser crystal was mounted on a Cu-holder using a silver paint for better heat removal, it was passively cooled. The crystal was placed at normal incidence in a nearly hemispherical cavity formed by a flat pump mirror (PM) coated for high transmission in the two pump ranges ($T > 97\%$ at 0.93–1.03 μm and $T > 80\%$ at 0.78–0.84 μm), and for high reflectance (HR) at 2.6–3.0 μm, and a concave output coupler (OC) having a radius of curvature of −75 mm and a transmission $T_{OC} = 1.5\%$ at the laser wavelength. The geometrical cavity length was ~75 mm. The airgap between the crystal and the PM was less than 0.5 mm. A tunable CW Ti:Sapphire laser (model 3900S, Spectra Physics) delivering up to 3.8 W at 968 nm and 4.1 W at 799 nm with excellent beam quality ($M^2 \approx 1$) was used as a pump source. The higher available pump power at 799 nm compensated the lower transmission of the PM at this wavelength. The pump radiation was focused into the laser element through the PM using an antireflection (AR) coated achromatic lens (focal length: f = 75 mm). Due to the differences in the position of the focus, pump beam quality and pump wavelengths, the pump beam radii averaged along the crystal length $< w_P >$ were considered. From the measurements performed by the optical knife method (at the $1/e^2$ level), they were determined to be $< w_P > = 63 \pm 5$ μm ($\lambda_P = 967.6$ nm) and 48 ± 5 μm ($\lambda_P = 799.2$ nm). The confocal parameter of the pump beam $2z_R$ was ~12 mm (in the crystal), i.e., being longer than the crystal thickness.

Optics EXPRESS

Two pump schemes were studied corresponding to the $^4I_{15/2} \rightarrow {}^4I_{11/2}$ (at ~0.97 μm) and $^4I_{15/2} \rightarrow {}^4I_{9/2}$ (at ~0.8 μm) Er^{3+} transitions, Fig. 1(a). A part of the unabsorbed pump beam was redirected back into the laser crystal due to a non-neglectable reflectivity of the OC at the pump wavelength (R = 12.2% at 968 nm and 40.0% at 799 nm). The single-pass pump absorption at the threshold pump power was determined from a pump-transmission experiment, $\eta_{abs(1-pass)}$ 76.9% ($^4I_{15/2} \rightarrow {}^4I_{11/2}$) and 50.1% ($^4I_{15/2} \rightarrow {}^4I_{9/2}$), and the total (double-pass) absorption was calculated accounting for the reflectivity of the OC and the Fresnel losses at the crystal surfaces, $\eta_{abs(2-pass)}$ = 78.6% ($^4I_{15/2} \rightarrow {}^4I_{11/2}$) and 59.2% ($^4I_{15/2} \rightarrow {}^4I_{9/2}$).

The non-absorbed (residual) pump was filtered out using a long-pass filter (LP1400, Spectrogon). The spectra of laser emission were measured using a fluoride fiber (Le Verre Fluoré) and a laser spectrum analyzer (Bristol, 771 series). The spatial profile of the laser mode and the beam radii in the far-field were measured using a camera (Pyrocam IIIHR, Ophir-Spiricon).

2.2. Laser performance

When pumping into the $^4I_{11/2}$ multiplet (λ_P = 967.6 nm), the Er:CaF_2 laser generated a maximum CW output power of 834 mW at 2800 nm with a slope efficiency η of 31.6% (versus the absorbed pump power) and a threshold P_{th} of only 24 mW, Fig. 2(a). This slope efficiency is only slightly below the Stokes limit, $\eta_{St,L} = \lambda_P/\lambda_L$ = 34.6%. The optical-to-optical efficiency η_{opt} with respect to the pump power incident on the crystal reached 23.2%. When pumping into the $^4I_{9/2}$ state (λ_P = 799.2 nm), the maximum output power was lower, namely 318 mW at 2800 nm with reduced η = 18.9% and slightly higher P_{th} of 33 mW. The reduction of the slope efficiency is mainly due to an additional energy loss originating from the non-radiative relaxation between the $^4I_{9/2}$ and $^4I_{11/2}$ states. The input-output dependences for both pump wavelengths were linear well above the laser threshold and no thermal roll-over nor crystal fracture were observed in the studied range of pump powers. A slight nonlinearity of the output dependence was observed near the threshold, as shown at the inset of Fig. 2(a).

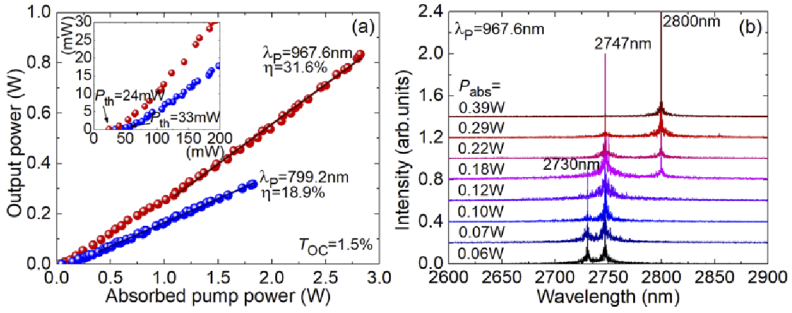

Fig. 2. Output performance of Er:CaF_2 lasers: (a) input-output dependences, η – slope efficiency, *inset* – a close look at the laser thresholds; (b) typical spectra of laser emission for λ_P = 967.6 nm measured at different pump powers, T_{OC} = 1.5%. The laser emission is unpolarized.

The laser emission was unpolarized. For both pump wavelengths, the emission wavelength experienced a red shift with increasing the pump power slightly above the laser threshold (from 2730 nm to 2747 nm and further to 2800 nm) and stabilized for high pump levels, as shown in Fig. 2(b) for the particular case of λ_P = 967.6 nm.

To explain this spectral behavior, one need to consider several factors. First, at a glance, the $^4I_{11/2} \rightarrow {}^4I_{13/2}$ laser transition is a quasi-four level one with no reabsorption. However, for Er^{3+} ions, there exist a strong resonant excited-state absorption (ESA) channel, $^4I_{13/2} \rightarrow {}^4I_{11/2}$, which may play a significant role considering a relatively high population of the metastable $^4I_{13/2}$ state.

Optics EXPRESS

In Fig. 3(a), we show the stimulated-emission (SE) cross-section, σ_{SE}, spectrum for the $^4I_{11/2} \rightarrow {}^4I_{13/2}$ transition, calculated using the Füchtbauer–Ladenburg (F-L) equation using a radiative lifetime $\tau_{rad} = 6.77$ ms and a luminescence branching ratio $B(JJ') = 16.3\%$ [23]. The maximum $\sigma_{SE} = 0.61\times10^{-20}$ cm^2 at 2730 nm. The broad and smooth profile SE cross-section spectrum is due to a strong ion clustering appearing for Er:CaF_2 crystals for doping levels >0.5 at.% leading to a significant inhomogeneous spectral broadening. By reciprocity method (RM), the ESA cross-sections, σ_{ESA}, were calculated, Fig. 3(a). The maximum $\sigma_{ESA} = 0.45\times10^{-20}$ cm^2 at 2730 nm.

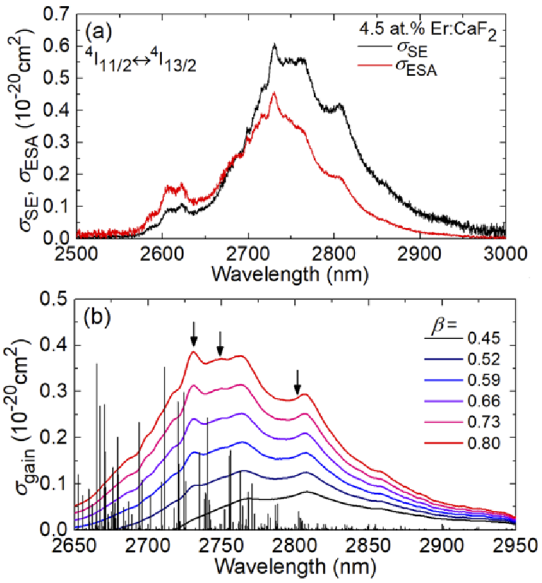

Fig. 3. Mid-infrared emission properties of Er^{3+} ions in the CaF_2 crystal: stimulated-emission (SE), σ_{SE}, and excited-state absorption (ESA), σ_{ESA}, cross-sections for the $^4I_{11/2} \leftrightarrow {}^4I_{13/2}$ transition (excluding water vapor absorption in the atmosphere); (b) gain cross-section, $\sigma_{gain} = \beta\sigma_{SE} - (1-\beta)\sigma_{ESA}$, spectra for different inversion ratios, $\beta = N_2/(N_1 + N_2)$, N_2 and N_1 are the populations of the upper and lower laser levels, respectively. *Vertical lines* – water vapor absorption in the atmosphere (according to HITRAN database), in arb. units.

Thus, by analogy to quasi-three-level lasers, the gain cross-sections, $\sigma_{gain} = \beta\sigma_{SE} - (1 - \beta)\sigma_{ESA}$, were calculated, where $\beta = N(^4I_{11/2})/(N(^4I_{11/2}) + N(^4I_{13/2}))$ is the inversion ratio and N are the manifold populations, as shown in Fig. 3(b). With decreasing β, several local peaks appear in the gain spectra centered at 2.73, 2.75, 2.76 and 2.81 μm, depending on the inversion level. Not all these wavelengths can be generated because of the structured water vapor absorption in the atmosphere spectrally overlapping with the mid-IR Er^{3+} luminescence, see Fig. 3(b). The possible lines are indicated by arrows, and they agree well with the laser spectra. The decrease of β with the pump power causing the observed red-shift of the laser wavelength is probably due to the pump-dependent ETU refilling the upper laser level.

The laser excitation curves (the dependence of the output power on the pump wavelength for a fixed incident pump power P_{inc}) were measured for both pump transitions, as shown in Fig. 4. When pumping into the $^4I_{11/2}$ and $^4I_{9/2}$ manifolds, lasing was achieved for λ_P in the ranges of 944.9–1014.8 nm and 781.0–834.2 nm, respectively. For comparison, in Fig. 4, we also show the corresponding absorption cross-section, σ_{abs}, spectra. The two sets of data agree well with each other, indicating that pumping into the absorption peak is desirable. For the $^4I_{15/2} \rightarrow {}^4I_{11/2}$

Optics EXPRESS

transition, $\sigma_{abs} = 1.85\times10^{-21}$ cm^2 at 967.6 nm and the absorption bandwidth (FWHM) is as broad as ~21 nm.

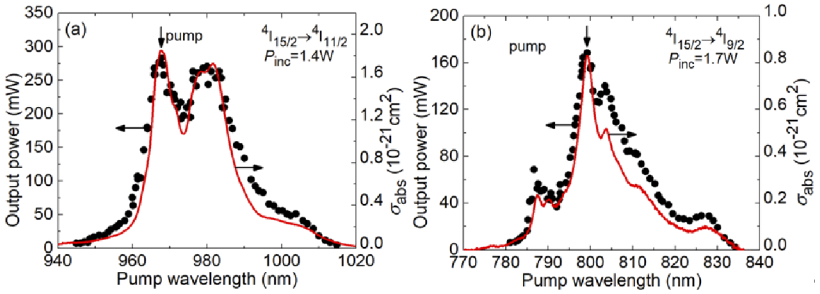

Fig. 4. Laser excitation curves for the Er:CaF_2 laser operating at ~2800 nm. The pump transitions are (a) $^4I_{15/2} \rightarrow {}^4I_{11/2}$ and (b) $^4I_{15/2} \rightarrow {}^4I_{9/2}$. *Symbols* – experimental data, *curves* - absorption cross-section, σ_{abs}, spectra.

The measured beam quality factors $M^2_{x,y}$ (x and y – horizontal and vertical directions) were close to 1 near the laser threshold and they increased to 2–2.5 at the maximum applied pump power. This mode behavior is common for quasi-four level lasers with no reabsorption in the unpumped regions of the gain medium which may provide additional spatial mode filtering. An example evaluation of the $M^2_{x,y}$ parameters for the Er:CaF_2 laser pumped at $\lambda_P = 967.6$ nm is shown in Fig. 5. It was performed according to the ISO-standard procedure. At an intermediate absorbed pump power P_{abs} of 0.75 W, they amounted to $M^2_x = 1.35$ and $M^2_y = 1.88$. At the inset of Fig. 5, we show the typical profile of the laser mode in the far-field. The mode shows only slight ellipticity.

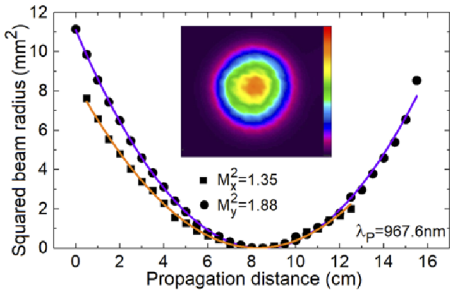

Fig. 5. Evaluation of the beam quality factors $M^2_{x,y}$ for the Er:CaF_2 laser, *inset* – typical far-field profile of the laser mode, $P_{abs} = 0.75$ W, $\lambda_P = 967.6$ nm.

3. Thermo-optic effects

3.1. Fractional heat loading

The fractional heat loading, i.e., the fraction of an absorbed pump power transferred into heat, $\eta_h = P_{heat}/P_{abs}$, is an important parameter for calculation of the optical power of the thermal lens, as well as for evaluation of the risk of thermal fracture. In the present work, it was measured by laser calorimetry (the gradient method) [24]. The change of the crystal temperature ΔT at its periphery was monitored as a function of time t when the pump was on ($0 < t < t_p$) and off ($t > t_p$, $t_p = 120$ s – pump pulse duration). For this, a sensitive thermocouple (Type K, Ni-Cr + Ni-Al) was attached to the crystal edge using a small amount of silver paint. The heating and the cooling curves were measured with a time step of 5 s and 10 s, respectively. By fitting the heating curve

Optics EXPRESS

as an exponential rise, the heating rate $(dT/dt)_h$ was determined at the moment of $t \approx 0.8t_p$. By fitting the cooling curve with an exponential decay, the cooling rate $(dT/dt)_c$ was determined at the moment of equal temperature, Fig. 6(a). Then, the fractional heat loading was calculated as $\eta_h = [(\Sigma m_i C_i)/P_{abs}]\ \ [(dT/dt)_h + (dT/dt)_c]$ [24], where m_i and C_i are the masses and the specific heats of the crystal ($m = 0.941$ g and $C = 0.858$ $Jg^{-1}K^{-1}$) and the Cu-holder ($m = 3.698$ g and $C = 0.385$ $Jg^{-1}K^{-1}$), respectively. Between the measurements, the laser crystal was left for ~10 min to return to the thermal equilibrium. Each measurement was repeated 3 times and the obtained η_h values were averaged.

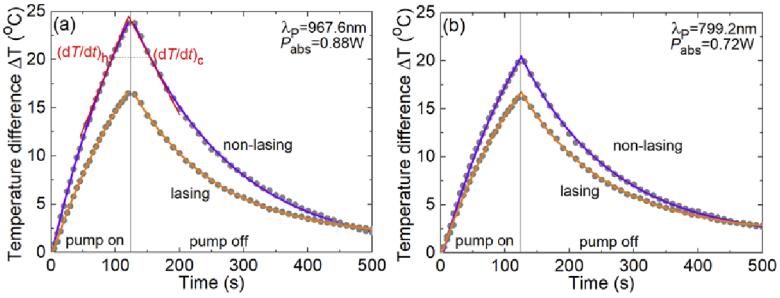

Fig. 6. Evaluation of the fractional heat loading η_h in a 4.5 at.% Er:CaF_2 laser crystal for lasing and non-lasing conditions. The pump wavelength λ_P is (a) 967.6 nm and (b) 799.2 nm. *Symbols* – experimental data, *curves* –exponential fits of rise and decay. *Vertical line* – the moment of switching off the pump (t_p), *dashed line* – temperature rise at $t = 0.8\ t_p$, *red lines* – heating and cooling slopes (see explanations in the text).

The measurements were done under lasing (L) and non-lasing (NL) conditions for both pump schemes, Fig. 6. From the measured heating curves, one can see that for the same absorbed pump power, under L conditions, the temperature rise at the boundary of the crystal (and the associated heat loading) are weaker than under NL conditions. Moreover, this effect is clearer for pumping into the $^4I_{11/2}$ state. The results on η_h are summarized in Fig. 7. When pumping into the $^4I_{11/2}$ state, $\eta_{h,L} = 52.0 \pm 2\%$ and $\eta_{h,NL} = 71.7 \pm 3\%$. When pumping into the $^4I_{9/2}$ state, both values increase and approach each other, $\eta_{h,L} = 64.1 \pm 4\%$ and $\eta_{h,NL} = 77.6 \pm 5\%$. The heat dissipation in Er:CaF_2 originates from multiphonon non-radiative (NR) relaxation and non-radiative transitions related to energy migration to defects and impurities from the excited-states directly populated via pump absorption, as well as populated via ETU. For the $^4I_{15/2} \rightarrow {}^4I_{9/2}$ pumping scheme, the heat loading both under L and NL conditions is increased due to an additional NR relaxation channel between the closely located $^4I_{9/2}$ and $^4I_{11/2}$ states.

Our experimental results agree well with the theoretical estimations by Pollnau [25] for Er:$LiYF_4$ crystals pumped into the $^4I_{11/2}$ Er^{3+} state with doping levels optimized for high slope efficiency [14], both qualitatively (the fractional heat loading is weaker under lasing conditions) and quantitatively.

Let us discuss in detail the mechanisms of heat generation in Er:CaF_2. First, the relevant energy-transfer processes have to be considered, see Fig. 1(a). These are two energy-transfer upconversion processes, ETU1 ($^4I_{13/2} + {}^4I_{13/2} \rightarrow {}^4I_{15/2} + {}^4I_{9/2}$) and ETU2 ($^4I_{11/2} + {}^4I_{11/2} \rightarrow {}^4I_{15/2} + {}^4F_{7/2}$), as well as a cross-relaxation process, CR ($^4S_{3/2} + {}^4I_{15/2} \rightarrow {}^4I_{9/2} + {}^4I_{13/2}$). Due to the strong ion clustering in Er:CaF_2 even at moderate doping levels, all the energy-transfer processes are expected to be more efficient than intrinsic decay from the long-living states, i.e., $^4I_{13/2}$, $^4I_{11/2}$ and thermally-coupled $^4S_{3/2}$+$^2H_{11/2}$ ones. Thus, the multiphonon NR relaxation from these states weakly contributes to heat generation. Still, for the levels quenched by fast NR relaxation, $^4I_{9/2}$, $^4F_{9/2}$ and $^4F_{7/2}$, its contribution to heat generation could be significant. As the $^4S_{3/2}$+$^2H_{11/2}$ states are mainly depleted by CR bypassing the $^4F_{9/2}$ state, the latter manifold has

Optics EXPRESS

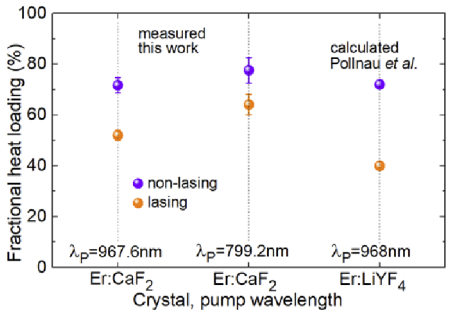

Fig. 7. A summary of measured values of the fractional heat loading η_h for a 4.5 at.% Er:CaF_2 laser crystal under lasing and non-lasing conditions. The calculated data for Er:$LiYF_4$ are given for comparison [25].

low population and does not contribute to heat release. Thus, two processes have to be considered: NR1 ($^4I_{9/2} \rightarrow {}^4I_{11/2}$) and NR2 ($^4F_{7/2} \rightarrow {}^4S_{3/2}$). Note that both of them are associated with an ETU process: NR1 follows ETU1 and NR2 follows ETU2. Under non-lasing conditions, the population of the $^4I_{11/2}$ level is not clamped by the threshold condition, and it greatly increases as compared to lasing conditions giving rise to an efficient ETU2 process followed by NR1, CR and NR2 processes. This explains higher η_h values observed under non-lasing conditions.

3.2. Thermal lensing

The thermal lens in the Er:CaF_2 crystal was studied under lasing conditions. To quantify it, first, the radii of the laser beam along two orthogonal directions were measured in the far-field at different pump powers. The measurements were performed at a certain difference from the OC (~9 cm) to reasonably increase the size of the output laser beam which gave better precision for further calculation of the thermal lens parameters. Then, the laser mode inside the cavity, as well as its propagation outside of the cavity were simulated using the ray transfer matrix formalism (ABCD) accounting for a thin ideal astigmatic thermal lens located in the center of the crystal, as well as the measured beam quality parameters $M^2_{x,y}$ of the laser radiation [26]. According to the ellipticity of the laser beam, two meridional planes of the thermal lens were established, denoted as "r" (A) and "θ" (B). Here, we use the same notations for cubic crystals as in the state-of-the-art works of Koechner [27] and Chenais *et al.* [28]. Note that these planes are not necessarily linked to the horizontal and vertical directions.

The beam radii of the laser mode measured as a function of the absorbed pump power for $\lambda_P = 799.2$ nm are shown in Fig. 8. The laser mode expands with the pump power indicating an action of a negative (divergent) thermal lens. The beam ellipticity is weak. In the same graph, we show the simulated dependences (curves) accounting for a pump-dependent thermal lens.

The results on the corresponding optical (refractive) power of the thermal lens $D = 1/f$ for both pump transitions are shown in Fig. 9. For the sake of correct comparison, the optical power of the thermal lens was plotted versus the on-axis absorbed pump intensity for a Gaussian beam, $I_{abs} = 2P_{abs}/(\pi < w_P >^2)$. The thermal lens in Er:CaF_2 is negative. Within the studied range of absorbed pump powers, the dependence of the optical power on I_{abs} can be reasonably good approximated with a linear law. Pollnau have simulated thermal lensing in Er:$LiYF_4$ and predicted a non-linear variation of the dioptric power, especially at high pump levels, mainly due to a temperature dependence of material parameters [25]. Such effects seem to be still weak for the studied lasers.

The slopes of these dependences are called the sensitivity factors, $M_{r(\theta)} = dD_{r(\theta)}/dI_{abs}$, showing the increase of the optical power due to a variation of the pump intensity by 1 kW/cm^2

Optics EXPRESS

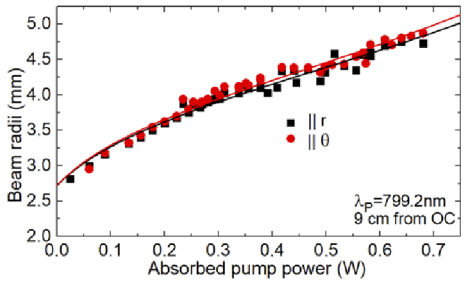

Fig. 8. Measured radii of the output beam from the Er:CaF_2 laser, $\lambda_P = 799.2$ nm, the distance from the OC is 9 cm, "r" and "θ" mark the semiaxes of the elliptical beam.

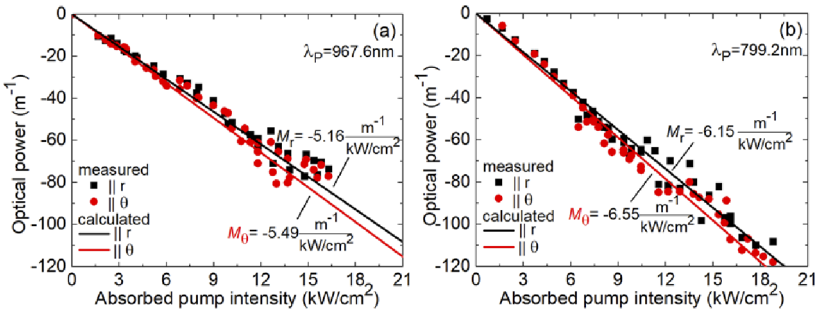

Fig. 9. Thermal lensing in the Er:CaF_2 laser crystal: optical power for principal meridional planes, *symbols* – experimental data, *lines* – calculation using Eq. (1), the calculated sensitivity factors (M) are indicated. The pump wavelength λ_P is (a) 967.6 nm and (b) 799.2 nm.

[29]. For $\lambda_P = 967.6$ nm, we obtained $M_r = -4.84$ and $M_\theta = -5.15$ [m^{-1}/(kW/cm^2)]. The thermal lens is weakly astigmatic: the astigmatism degree, $S/M = |M_\theta - M_r|/|M_\theta|$, is only ~6%. For $\lambda_P = 799.2$ nm, the thermal lens becomes stronger owing to the stronger heat dissipation, $M_r = -6.15$ and $M_\theta = -6.49$ [m^{-1}/(kW/cm^2)].

For completeness, we also list the sensitivity factors of the thermal lens versus the absorbed pump power (note that they should not be directly compared due to the slightly different mean pump spot radii), $M_r = -77.7$ and $M_\theta = -82.7$ [m^{-1}/W] ($\lambda_P = 967.6$ nm) and $M_r = -133.7$ and $M_\theta = -142.3$ [m^{-1}/W] ($\lambda_P = 799.2$ nm).

At the maximum applied pump power, the focal length of the thermal lens ($f = 1/D$) is as short as −12. . . −13 mm ($\lambda_P = 967.6$ nm) and −8. . . −9 mm ($\lambda_P = 799.2$ nm). The main reasons for such a strong lens are the following: (i) high fractional heat loading for Er^{3+} ions (e.g., as compared to Yb^{3+} ones [28]) and (ii) small pump spot size used in the present work together with a Gaussian profile of the pump beam (as compared to typical values for diode-pumped lasers). The latter is beneficial for the thermal lens measurements as it allowed us to observe stronger (and more easily detectable) effect of the thermal lens on the laser characteristics. Despite the observed relatively short focal lengths of the thermal lens, the laser cavity remained stable. The calculated stability limit of such a cavity expressed in the focal length of a divergent thermal lens is $f = -4$ mm.

The optical power of the thermal lens in a longitudinally pumped laser element made of a cubic crystal in the "plane stress" approximation is given by [28]:

$$D_{r(\theta)} = \frac{\eta_h P_{abs}}{\pi \langle w_P \rangle^2 \kappa} (dn/dT + 2n^3 \alpha C_{r(\theta)} + (1+\nu)(n-1)\alpha), \quad (1)$$

Optics EXPRESS

where κ is the thermal conductivity, n is the refractive index and dn/dT is the thermo-optic coefficient, α is the coefficient of thermal expansion, ν is the Poisson ratio and $C_{r(\theta)}$ are the so-called photoelastic constants [27]. The three terms in parentheses correspond to three main effects contributing to the thermal lens formation: (i) temperature dependence of the refractive index under zero strains, $\varepsilon = 0$ (expressed by the dn/dT term), (ii) the photo-elastic effect (expressed by the photo-elastic term, $P_{PE,r(\theta)}$) and (iii) macroscopic bulging of crystal end faces (expressed by the end-bulging term, Q_{dist}), respectively. The whole expression in parentheses is called the "generalized" thermo-optic coefficient $\chi_{r(\theta)} = \mathrm{d}n/\mathrm{d}T + P_{PE,r(\theta)} + Q_{dist}$. Equation (1) considers the case of a Gaussian spatial profile of the pump beam. The $C_{r(\theta)}$ values for an optically isotropic material under "plane stress" approximation are given by [28]:

$$C_r = \frac{-(1+\nu)(9p_{11}+15p_{12})}{48}, \tag{2a}$$

$$C_\theta = \frac{-(1+\nu)(7p_{11}+17p_{12}-8p_{44})}{48}, \tag{2b}$$

where p_{ij} are the elasto-optical coefficients. The set of material parameters involved in the thermal lens simulation is provided in Table 2 [30,31].

Table 2. Material Parameters of Er:CaF_2 Involved in the Thermal Lens Calculation

Parameter	Value [30,31]	Parameter	Value [31]	Parameter	Value (calculated)
n	1.419	p_{11}	0.038	$P_{PE,r}$ [10^{-6} K^{-1}]	−11.79
dn/dT [10^{-6} K^{-1}]	−8.5	p_{12}	0.266	$P_{PE,\theta}$ [10^{-6} K^{-1}]	−12.48
α [10^{-6} K^{-1}]	18.9	p_{44}	0.0254	Q_{dist} [10^{-6} K^{-1}]	9.58
ν	0.21	C_r	−0.109	χ_r [10^{-6} K^{-1}]	−10.71
κ [$Wm^{-1}K^{-1}$]	5.4	C_θ	−0.116	χ_θ [10^{-6} K^{-1}]	−11.40

Note that the expression for the end-bulging term, $Q_{dist} = (1+\nu)(n-1)\alpha$, is strictly valid for an infinitely thin crystal [28] (or at least in the case when the heat loading is strongly localized near the input crystal face due to a strong pump absorption). Cousins showed that for a laser element (rod) with a length / diameter ratio of about 1.5, this expression overestimates the actual bulging by about 1/3 [32]. Thus, it should be taken as an upper limit estimation of end bulging and stronger negative thermal lens is expected in long uniformly pumped Er:CaF_2 crystals.

The calculated sensitivity factors of the thermal lens are the following: $M_r = -5.16$ and $M_\theta = -5.49$ [m^{-1}/(kW/cm^2)] for $\lambda_P = 967.6$ nm and $M_r = -6.15$ and $M_\theta = -6.55$ [m^{-1}/(kW/cm^2)] for $\lambda_P = 799.2$ nm and $S/M = 6\%$. These values agree well with the experimental ones confirming the correctness of the measured fractional heat loading. Thermal lens in Er:CaF_2 is divergent mainly because of the negative thermo-optic coefficient, dn/dT, and large and negative photo-elastic terms, $P_{PE,r(\theta)}$, see Table 2. Negative thermal lens is common for fluorite-type crystals [33].

The determined parameters of the thermal lens in Er:CaF_2 crystals are relevant for the design of power-scalable mid-infrared lasers based on this gain material, including diode-pumped ones. In this case, the parameters of the thermal lens can be easily recalculated from our data by considering the changed pump spot size. The knowledge of the thermal lens of a laser element is crucial for determining the stability of a designed laser cavity, as well as matching of the pump and laser modes in the laser element with increasing the pump power.

4. Conclusion

To conclude, Er:CaF_2 crystals are promising for CW low-threshold mid-infrared lasers emitting at ~2.8 μm. In the present paper, we report on the highest output power ever extracted from this

Optics EXPRESS

type of lasers (0.84 W at 2800 nm), owing to a high optical quality of the crystal and a moderate doping level (4.5 at.% Er). The latter maintains reasonably good thermal properties (which deteriorate fast with the doping level) and at the same time ensures efficient ETU between the Er^{3+} ions owing to their strong clustering. The power scaling capabilities and thermo-optical behavior of Er:CaF_2 are directly compared for two pump schemes, namely pumping into the $^4I_{11/2}$ and $^4I_{9/2}$ levels. Direct excitation into the upper laser level provides higher slope efficiency, lower fractional heat loading under lasing conditions and, consequently, weaker thermal lens. The latter is found to be negative (divergent) for the Er:CaF_2 crystal due to the negative thermo-optic coefficient and large and negative contribution of the photo-elastic effect. The mechanisms of heat generation in Er:CaF_2 are discussed. The achieved laser slope efficiency (31.6%, pumping into the $^4I_{11/2}$ state) is only slightly lower than the Stokes limit indicating a room for further improvement via a careful optimization of the Er^{3+} doping level which determine the ratio of ETU probabilities. The smooth and broad gain spectra of Er^{3+} ions in CaF_2 make this crystal particularly attractive for generation of ultrashort pulses.

Funding. Agence Nationale de la Recherche (ANR-19-CE08-0028); Région Normandie (Chaire d'excellence "RELANCE").

Disclosures. The authors declare no conflicts of interest.

Data availability. Data underlying the results presented in this paper are not publicly available at this time but may be obtained from the authors upon reasonable request.

References

1. M.-E. Kim, D.-J. Jeoung, and K.-S. Kim, "Effects of water flow on dental hard tissue ablation using Er:YAG laser," J Clin. Laser Med. Surg. **21**(3), 139–144 (2003).
2. T. S. Alster, "Clinical and histologic evaluation of six erbium:YAG lasers for cutaneous resurfacing," Lasers Surg. Med. **24**(2), 87–92 (1999).
3. N. M. Fried, Z. Tesfaye, A. M. Ong, K. H. Rha, and P. Hejazi, "Optimization of the Erbium:YAG laser for precise incision of ureteral and urethral tissues: in vitro and in vivo results," Lasers Surg. Med. **33**(2), 108–114 (2003).
4. R. C. Stoneman, J. G. Lynn, and L. Esterowitz, "Direct upper-state pumping of the 2.8 µm Er^{3+}:YLF laser," IEEE J. Quantum Electron. **28**(4), 1041–1045 (1992).
5. B. J. Dinerman and P. F. Moulton, "3-µm cw laser operations in erbium-doped YSGG, GGG, and YAG," Opt. Lett. **19**(15), 1143–1145 (1994).
6. M. Pollnau, T. Graf, J. E. Balmer, W. Lüthy, and H. P. Weber, "Explanation of the cw operation of the Er^{3+} 3-µm crystal laser," Phys. Rev. A **49**(5), 3990–3996 (1994).
7. T. Sandrock, D. Fischer, P. Glas, M. Leitner, M. Wrage, and A. Diening, "Diode-pumped 1-W Er-doped fluoride glass M-profile fiber laser emitting at 2.8 µm," Opt. Lett. **24**(18), 1284–1286 (1999).
8. G. A. Newburgh and M. Dubinskii, "Power and efficiency scaling of Er:ZBLAN fiber laser," Laser Phys. Lett. **18**(9), 095102 (2021).
9. T. Jensen, A. Diening, G. Huber, and B. H. T. Chai, "Investigation of diode-pumped 2.8-µm Er:$LiYF_4$ lasers with various doping levels," Opt. Lett. **21**(8), 585–587 (1996).
10. M. Pollnau, W. Lüthy, H. P. Weber, T. Jensen, G. Huber, A. Cassanho, H. P. Jenssen, and R. A. McFarlane, "Investigation of diode-pumped 2.8-µm laser performance in Er:BaY_2F_8," Opt. Lett. **21**(1), 48–50 (1996).
11. L. Basyrova, P. Loiko, J.-L. Doualan, A. Benayad, A. Braud, C. Labbe, and P. Camy, "Er:KY_3F_{10} laser at 2.80 µm," Opt. Lett., *accepted* (2021).
12. C. Labbe, J. L. Doualan, P. Camy, R. Moncorgé, and M. Thuau, "The 2.8 µm laser properties of Er^{3+} doped CaF_2 crystals," Opt. Commun. **209**(1-3), 193–199 (2002).
13. T. T. Basiev, Y. V. Orlovskii, M. V. Polyachenkova, P. P. Fedorov, S. V. Kuznetsov, V. A. Konyushkin, V. V. Osiko, O. K. Alimov, and A. Y. Dergachev, "Continuously tunable cw lasing near 2.75 µm in diode-pumped Er^{3+}:SrF_2 and Er^{3+}:CaF_2 crystals," Quantum Electron. **36**(7), 591–594 (2006).
14. C. Wyss, W. Lüthy, H. P. Weber, P. Rogin, and J. Hulliger, "Emission properties of an optimised 2.8 µm Er^{3+}:YLF laser," Opt. Commun. **139**(4-6), 215–218 (1997).
15. A. Y. Dergachev, J. H. Flint, and P. F. Moulton, "1.8-W CW Er:YLF diode-pumped laser," in *Conference on Lasers and Electro-Optics*, S. Brueck, R. Fields, M. Fejer, and F. Leonberger, eds., OSA Technical Digest (Optical Society of America, 2000), paper CFA2.
16. S. Renard, P. Camy, A. Braud, J. L. Doualan, and R. Moncorgé, "CaF_2 doped with Tm^{3+}: A cluster model," J. Alloys Compd. **451**(1-2), 71–73 (2008).
17. V. Petit, P. Camy, J.-L. Doualan, X. Portier, and R. Moncorgé, "Spectroscopy of Yb^{3+}:CaF_2: from isolated centers to clusters," Phys. Rev. B **78**(8), 085131 (2008).

Optics EXPRESS

18. W. Ma, L. Su, X. Xu, J. Wang, D. Jiang, L. Zheng, X. Fan, C. Li, J. Liu, and J. Xu, "Effect of erbium concentration on spectroscopic properties and 2.79 μm laser performance of Er:CaF_2 crystals," Opt. Mater. Express **6**(2), 409–415 (2016).
19. W. Ma, X. Qian, J. Wang, J. Liu, X. Fan, J. Liu, L. Su, and J. Xu, "Highly efficient dual-wavelength mid-infrared CW laser in diode end-pumped Er:SrF_2 single crystals," Sci. Rep. **6**(1), 36635 (2016).
20. C. Li, J. Liu, S. Jiang, S. Xu, W. Ma, J. Wang, X. Xu, and L. Su, "2.8 μm passively Q-switched Er:CaF_2 diode-pumped laser," Opt. Mater. Express **6**(5), 1570–1575 (2016).
21. J. Šulc, M. Němec, R. Švejkar, H. Jelínková, M. E. Doroshenko, P. P. Fedorov, and V. V. Osiko, "Diode-pumped Er:CaF_2 ceramic 2.7 μm tunable laser," Opt. Lett. **38**(17), 3406–3409 (2013).
22. J. Liu, X. Feng, X. Fan, Z. Zhang, B. Zhang, J. Liu, and L. Su, "Efficient continuous-wave and passive Q-switched mode-locked Er^{3+}:CaF_2–SrF_2 lasers in the mid-infrared region," Opt. Lett. **43**(10), 2418–2421 (2018).
23. C. Labbé, J. L. Doualan, R. Moncorgé, A. Braud, and P. Camy, "Excited-state absorption and fluorescence dynamics in Er:CaF_2," J. Lumin. **200**, 74–80 (2018).
24. U. Willamowski, D. Ristau, and E. Welsch, "Measuring the absolute absorptance of optical laser components," Appl. Opt. **37**(36), 8362–8370 (1998).
25. M. Pollnau, "Analysis of heat generation and thermal lensing in erbium 3-μm lasers," IEEE J. Quantum Electron. **39**(2), 350–357 (2003).
26. P. Loiko, S. Manjooran, K. Yumashev, and A. Major, "Polarization anisotropy of thermal lens in Yb:$KY(WO_4)_2$ laser crystal under high-power diode pumping," Appl. Opt. **56**(10), 2937–2945 (2017).
27. W. Koechner, *Solid-state laser engineering* (Springer, New York 2006).
28. S. Chenais, F. Druon, S. Forget, F. Balembois, and P. Georges, "On thermal effects in solid-state lasers: the case of ytterbium-doped materials," Prog. Quantum Electron. **30**(4), 89–153 (2006).
29. P. A. Loiko, K. V. Yumashev, N. V. Kuleshov, V. G. Savitski, S. Calvez, D. Burns, and A. A. Pavlyuk, "Thermal lens study in diode pumped N_g- and N_p-cut Nd:$KGd(WO_4)_2$ laser crystals," Opt. Express **17**(26), 23536–23543 (2009).
30. I. H. Malitson, "A Redetermination of Some Optical Properties of Calcium Fluoride," Appl. Opt. **2**(11), 1103–1107 (1963).
31. F. Druon, S. Ricaud, D. N. Papadopoulos, A. Pellegrina, P. Camy, J. L. Doualan, R. Moncorgé, A. Courjaud, E. Mottay, and P. Georges, "On Yb:CaF_2 and Yb:SrF_2: review of spectroscopic and thermal properties and their impact on femtosecond and high power laser performance [Invited]," Opt. Mater. Express **1**(3), 489–502 (2011).
32. A. Cousins, "Temperature and thermal stress scaling in finite-length end-pumped laser rods," IEEE J. Quantum Electron. **28**(4), 1057–1069 (1992).
33. M. Chen, P. Loiko, J. M. Serres, S. Veronesi, M. Tonelli, M. Aguiló, F. Díaz, J. E. Bae, T. G. Park, F. Rotermund, S. Dai, Z. Chen, U. Griebner, V. Petrov, and X. Mateos, "Fluorite-type Tm^{3+}:KY_3F_{10}: A promising crystal for watt-level lasers at ~1.9 μm," J. Alloys Compd. **813**, 152176 (2020).